Performance of the 0-padding Optimal Filter Method in Non-linear Gain Calibration

Michael C. Witthoeft[a,b], Stephen J. Smith[a], Edoardo Cucchetti[c], Nicolás Cardiel[d,e], M. Teresa Ceballos[f], Beatriz Cobo[f], Joseph S. Adams[a,g], Simon R. Bandler[a], James A. Chervenak[a], Fred M. Finkbeiner[a,h], Joshua D. Fuhrman[a,g], Samuel V. Hull[a,i], Richard L. Kelley[a], Caroline A. Kilbourne[a], F. Scott Porter[a], Kazuhiro Sakai[a,g], Nicholas A. Wakeham[a,g]

***Abstract*—The focal-plane detector, the X-ray Integral Field Unit (X-IFU), on-board ESA's Athena space telescope is a transition edge sensor (TES) microcalorimeter array with 1.5k pixels, designed to provide spatially-resolved, high-resolution spectroscopy over the energy range 0.2-12 keV. The onboard event processor uses a digital optimal filter to determine the pulse-height of the measured current pulse from every X-ray photon striking the array. A modified optimal filter called the 0-padding filter has recently been proposed. This is a truncated version of the standard optimal filter and has been shown to provide comparable energy resolution but with the benefit of reduced computational expense. Whereas the standard optimal filter has zero integral and is not sensitive to variations in the DC level of the measured signal, the integral of the 0-padded version is non-zero and thus is more sensitive to fluctuations in DC signal over time. In this work, we explore the effect of 0-padding on the energy scale calibration using data from 250-pixels in a prototype Athena X-IFU array, measured over the range 1.3-12 keV.**

***Index Terms*—Microcalorimeter, imaging spectrometer, transition-edge sensor**

I. Introduction

ATHENA [1] is an X-ray telescope selected by ESA for launch in the late 2030s. It will feature a high-resolution imaging spectrometer, the X-ray Integral Field Unit (X-IFU) [2], featuring an array of 1504 TES microcalorimeter pixels developed at NASA/GSFC [3]. X-ray events are partially processed on-board the telescope via an optimal filter [4]. The large number of pixels and high event count rates lead to a lot of computation required by the on-board processor. The 0-padding method [5] is a variation of the optimal filter method which needs fewer computational resources and has demonstrated comparable energy resolution as the standard method when using simple energy calibration methods. In this work, we explore the consequences of the 0-padding method on the determination of absolute photon energies using calibration techniques similar to what is intended for the Athena mission [6], [7] and determine the impact, if any, on the ultimate energy resolution of the detector. We focus our attention on the final resolution of the calibrated spectrum rather than the accuracy of the energy scale, because that is where the effects of 0-padding are most strongly felt. However, a good energy resolution is strongly correlated with accurate absolute energies, particularly when applying non-linear calibration methods and examining co-added spectra.

The data [6] used in this work are taken from a prototype kilo-pixel array with ∼200 active pixels using 8-column by 32-row TDM (time division multiplexing) [8], [9]. Previously [6], [7], we have demonstrated the ability to correct the gain scale due to various drifts in the environment using the standard optimal filter. In this report, we use the same data sets to compare results with the 0-padding optimal filter approach.

We construct polynomial gain scales using 15 Kα lines (Figure 1) from Mg (1.3 keV) to Zn (9 keV) generated using a rotating target source (RTS) [10] under a variety of operating conditions with varying bath temperatures and magnetic fields. We use the Cr Kα and Cu Kα lines from the RTS source to track and correct variations in the gain due to time-dependent drifts in the detector environment. For Athena, an on-orbit modulated X-ray source (MXS) [2] will provide these same lines for tracking the gain variation.

II. 0-padding

Optimal filtering [4] is a technique for measuring the height of an X-ray pulse accounting for the noise signature of the detector. The pulse height of an event is computed as the dot product of the pulse record with the optimal filter. 0-padding (ZP) is a new technique [5] where the optimal filter is truncated so that fewer samples are used in the dot product. Initially, ZP was explored as a method to save computation time. But it was discovered that it can also improve the energy resolution by removing the noise contribution to the pulse height calculation

This material is based upon work supported by NASA under award number 80GSFC21M0002. N. Cardiel, M. T. Ceballos, and B. Cobo acknowledge Grant PID2021_122955OB-C41 funded by MCIN/AEI/10.13039/501100011033 and by "ERDF A way of making Europe". Corresponding author: M. C. Witthoeft, email: michael.c.witthoeft@nasa.gov.

[a]NASA Goddard Space Flight Center, Greenbelt, MD 20771, USA

[b]ADNET Systems, Inc., Bethesda MD 20817, USA

[c]Centre National d'Etudes Spatiales (CNES), 18 Av. Edouard Belin 31400 Toulouse, France

[d]Departamento de Física de la Tierra y Astrofísica, Facultad de CC. Físicas, Universidad Complutense de Madrid, Plaza Ciencias 1, Madrid E-28040, Spain

[e]Instituto de Física de Partículas y del Cosmos, IPARCOS, Facultad de CC. Físicas, Universidad Complutense de Madrid, Plaza Ciencias 1, Madrid E-28040, Spain

[f]Instituto de Física de Cantabria, CSIC-Universidad de Cantabria, Avda Los Castros s/n, Santander E-39005, Spain

[g]Center for Research and Exploration in Space Science and Technology, University of Maryland Baltimore County, Baltimore, MD 21250, USA

[h]Sigma Space Corp./Hexagon US Federal, 4600 Forbes Blvd., Lanham, MD 20706, USA

[i]Department of Astronomy, University of Maryland College Park, MD 20742, USA

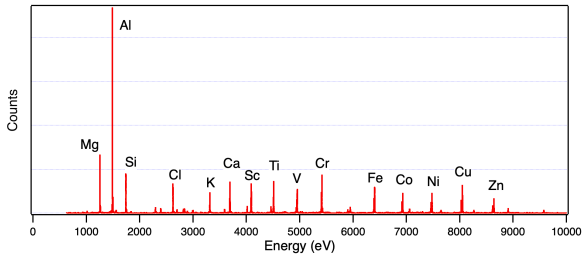

Fig. 1. Example spectrum showing the RTS Kα lines used to construct the energy gain scales.

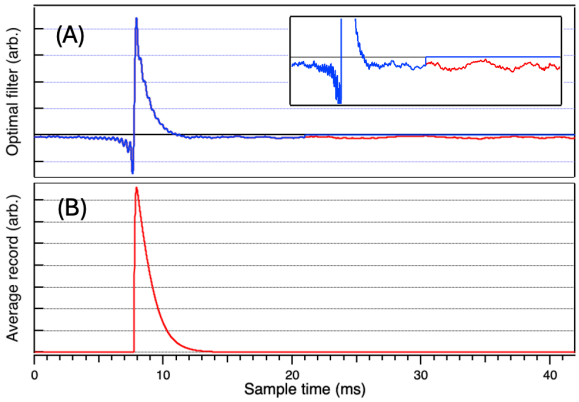

Fig. 2. (A) Optimal filters used in this work: full-length (red) and 0-padded (blue); the inset is a vertical zoomed view showing that the 0-padded filter is set to zero for the last half of the record. (B) The average pulse record used in the construction of the full-length optimal filter.

in the region of the record where the X-ray pulse signal is vanishingly small. In Section III, we will describe how we correct for the missing part of the dot product in a way that does not reintroduce the sample variance.

In Figure 2A, we show the optimal filters used in this work. The full-length filter (FL) was computed using an average pulse record (bottom panel) constructed from the Cr Kα pulse records in our reference data set ($T_{bath} = 50$ mK and zero magnetic field). It has 8192 samples measured at a rate of ~ 195.3 kHz and a pre-trigger region of 1500 samples. The 0-padded filter has 4096 samples with the same pre-trigger length.

In Figure 3, we show the standard deviation of optimally filtered pulse heights from 970 noise records as a function of the ZP filter length. They are in good agreement with the predicted values [5] of $\sigma = \sqrt{\sum_i^n f_i^2}$ where f_i is the discretized optimal filter and n the length of the ZP filter. By truncating the filter after 4096 samples, ZP omits the dispersion in the region of the record contributing little to the pulse height measurement.

However, due to the truncation, ZP filters have an increased sensitivity to the DC level of the pulse record. The FL filter is normalized to have an area of zero. In the frequency domain, this is equivalent to the 0-frequency bin being set to zero, implying no dependence on the DC level. After truncation, the ZP filter no longer has zero area, so any variation of the DC level during the measurement (due to drifts in the operating conditions of the detector or readout electronics) can affect the

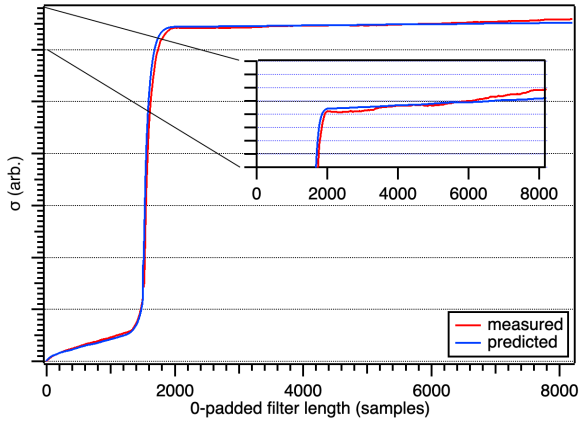

Fig. 3. Standard deviation of optimally-filtered pulse heights from noise records as a function of the ZP filter length (red) compared with the predicted standard deviation [5] (blue).

measured pulse heights. This complicates energy calibration, and possibly has a resolution cost because we need to track how the DC level evolves in time sufficiently well to correct for its effects on the pulse heights.

III. DC LEVEL SENSITIVITY

Using the FL filter ($N = 8192$ samples), the pulse height of an event, x, is the dot product of the pulse record, $\mathbf{R}$, and the optimal filter: $x = \langle \mathbf{R}|\mathbf{f}\rangle$. With ZP, we truncate the optimal filter to $n = 4096$ samples which is equivalent to terminating the dot product early. The ZP pulse heights can be written as $x_n = \langle \mathbf{R}|\mathbf{f}\rangle_n$ where the n subscript on the *ket* denotes stopping the dot product sum at the n'th index.

Pulse records can be decomposed as $\mathbf{R} = \mathbf{r} + b$ where b is the DC level for the event and $\mathbf{r}$ is the pulse record with the DC level subtracted. We call the DC level for an event its baseline which is computed as the average signal over the pre-trigger region and considered fixed for a single X-ray event. The variation of the baseline level over time is referred to as the baseline drift. The ZP pulse height of an event can then be expressed as

$$x_n = \langle \mathbf{r}|\mathbf{f}\rangle_n + b\sum_i^n f_i + x_s, \tag{1}$$

where the FL pulse height is regained by letting $n \to N$. The final term, x_s, is an offset used to align the ZP spectrum with the FL spectrum and serves to compensate for the pulse height magnitude we lose by truncating the ZP filter. The options for determining this offset and their consequences will be discussed in Section V.

In the FL case, the 2nd term in Equation 1 is identically zero due to the normalization of the full-length optimal filter. With ZP, however, the sum of the filter is non-zero and the ZP pulse heights become linearly dependent on the baseline (see Figure 4). This additional baseline dependence exacerbates the time-dependent drift of the pulse heights compared to the FL results. Figure 5A shows the optimally filtered pulse heights for Cr Kα versus time for the FL and ZP methods from a single representative pixel along with the calculated trend of the line

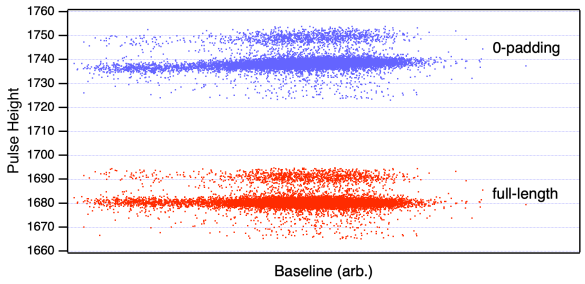

Fig. 4. Pulse heights as a function of baseline for Al Kα events from the full-length (red) and 0-padded (blue) results. We see a small change in the slope of the 0-padded events due to the 2nd term in Equation 1.

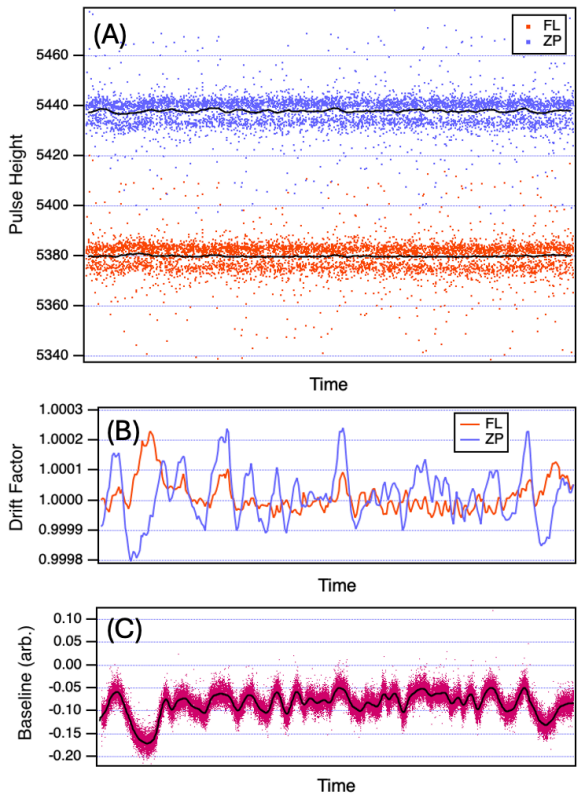

Fig. 5. (A) Comparison of pulse heights from the Cr Kα line as a function of time using FL (red) and ZP (blue); (B) corresponding drift scaling factors [derived from the black curves in (A)]. (C) Event baselines as a function of time (magenta) and the average trend (black). The features in the (C) can be seen to affect the drift scaling factors from the ZP calculation in (B).

centroid. The corresponding drift correction scale factors are shown in Figure 5B where some of the features in the ZP drift can be seen to originate from the baseline drift (Figure 5C). Left uncorrected, these larger fluctuations will degrade the resolution. We will describe our method for correcting for the baseline drift in Section V.

IV. Energy Calibration Method

To obtain photon energies from the optimally filtered pulse heights, we need to perform an energy calibration. This can be done with a single gain curve measured under the same environmental conditions (e.g. bath temperature) as the data set. In general, however, we do not know the exact conditions of the

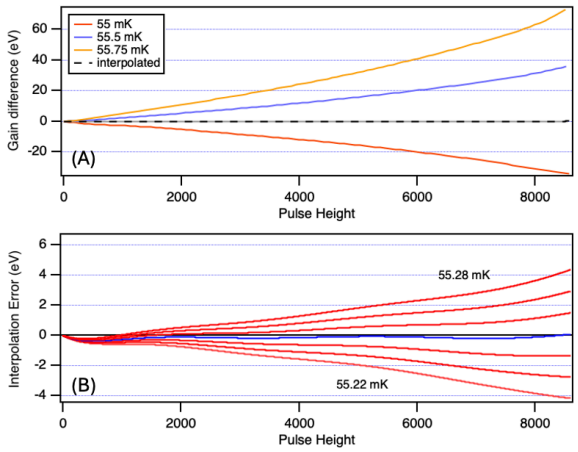

Fig. 6. (A) The difference between three reference gain scales (55, 55.5, and 55.75 mK) and the gain scale computed for the data set taken at 55.25 mK. The dashed line shows the error in the gain scale interpolated using the reference gains. All gain scales were derived using the full-length filter. (B) Errors in interpolated gains computed at 7 equally-spaced effective temperatures from 55.22 to 55.28 mK; the blue curve is 55.25 mK.

detector when the measurements are taken. So, instead, we use multiple gain curves taken under various, controlled conditions to calibrate our data. Using one or two calibration lines, we measure effective environmental parameters and obtain new gain curves by interpolating the reference set of gain curves with 2nd-order Lagrange polynomials. To correct on a single parameter [11], e.g. T_{bath}, we require three reference gain scales and a single fiducial line. This approach can be extended to two parameters [12] (e.g. T_{bath} and B-field) by using six reference gains, a fiducial line and the event baselines. In this work, for the 2-parameter calibration, we deviate slightly from Ref. [12] in that we use two fiducial lines instead of using the baseline. The effective parameters are measured as a function of time to account for drifts in the line positions throughout the data collection.

In Figure 6A, we show the difference between three reference gain scales (T_{bath} = 55, 55.5, and 55.75 mK) with the gain scale computed for a data set taken at 55.25 mK, all derived from the FL pulse heights. This set of gains can be used for the 1-parameter calibration method. By fitting a 2nd-order polynomial to the reference gain scales at each pulse height, we can obtain an interpolated gain scale at any temperature. In Figure 6B, we show the interpolation error at several effective temperatures compared to the measured gain scale at 55.25 mK. The gain scale interpolated at 55.25 mK is accurate to within 0.5 eV over the whole spectral range (blue curve in the figure).

The reference gain scales are also used to deduce the effective environmental parameter values from the measured pulse height of a calibration line. As described in Ref. [11], the pulse height of a calibration line can be interpolated onto the expected positions of that line from each reference gain curve to yield the effective parameter value for the data set. By measuring the position of the line as a function of time, we can use this procedure to obtain time-dependent parameters. The time-dependent line positions are measured

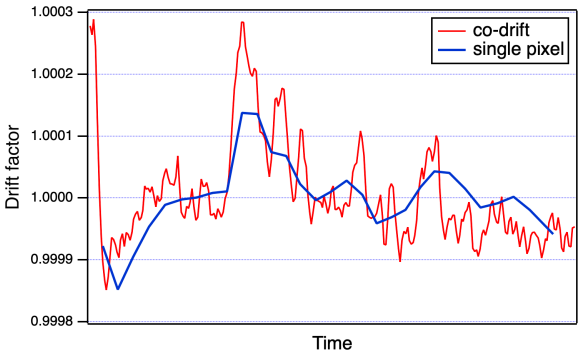

Fig. 7. Comparison of time-dependent drift correction factors computed using data from a single pixel (blue) vs. co-drifting across a 32-pixel column (red).

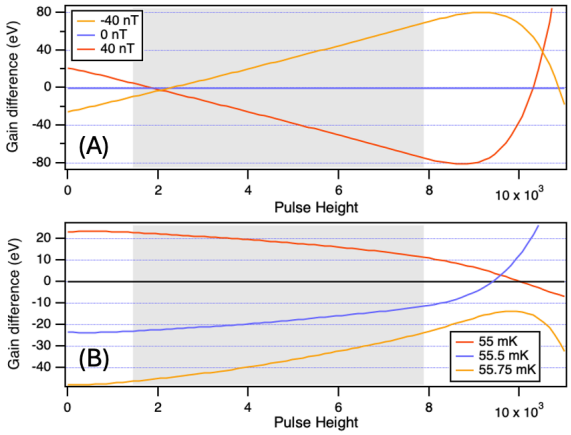

Fig. 8. (A) The difference between the ZP gain scales over a varying magnetic field (-40 nT and +40 nT compared against 0 nT). The gains do not continue to diverge above 8000 due to extrapolation errors in the polynomial gain curves. (B) The difference between three ZP gain scales (55 mK, 55.5 mK, and 55.75 mK) with the 55.25 mK gain scale. The crossover point occurs around a pulse height of 10,000 but extrapolation errors prevent all of them from crossing. The grey area shows the calibration region.

by grouping adjacent events from a single line complex and fitting the theoretical line shape to the histogram of grouped pulse heights. There is a fundamental trade-off on the size of these fitting groups. On one hand, large groups provide good statistics needed for an accurate fit. However, small groups are necessary to track rapid changes of the line centroid over time.

Typically, the drifts in the line centroid are measured for each pixel separately. However, for the data sets in this study, we get better results by grouping events from many pixels together. We call this co-drifting, but it is also referred to as pixel grouping [7]. The co-drifting procedure is: 1) we scale down the pulse heights from each pixel by the time-averaged centroid of the calibration line, 2) perform the drift fitting on the merged data set, and 3) undo the per-pixel scaling. We have found that pixels within the same column (32 pixels per column) have a similar time-dependent behavior. With co-drifting, we are able to get good statistics for the fit and still accurately track the time dependence of the line centroid. In Figure 7, we show the much improved time fidelity of the drift scaling factors from co-drifting compared against a single-pixel calculation. Furthermore, the co-drifted results use 1000 events per fitting group vs 300 per group in the single-pixel case, leading to better centroid fitting. For all of the results in this work (FL and ZP), co-drifting has been used for calibration.

V. Gain Crossover Point

When computing the ZP pulse heights using Eq. 1, there is an offset, x_s, we use to compensate for the missing contribution to the pulse height dot product due to the truncated filter. The simplest choice is to use a fixed offset which is applied to all data sets regardless of the environmental conditions. For example, we can choose an offset that aligns the ZP pulse heights of the Cr Kα line to agree with those using the FL filter for the reference data set ($T_{\text{bath}} = 55$mK and zero magnetic field). Such an offset, however, causes the gain curves measured under different conditions to overlap at a non-zero energy; we call this a crossover point.

In Figure 8A, ZP gains over a varying magnetic field (± 40 nT) are compared with the gain with no B-field applied. All of the gains give the same energy at a pulse height of $\sim$2000 units. This crossover point implies an insensitivity of the gain to the B-field meaning that an effective magnetic field value cannot be inferred from a fiducial line in the vicinity of the crossover point. So, when calibrating this case, we are confined to using lines sufficiently above the crossover point to distinguish the B-field values computed from each gain.

For the case of varying bath temperatures (Figure 8B), the crossover point occurs outside of the calibration region at high energies. So, unlike the varying magnetic field case, there are no restrictions on what energies we can use for calibration. However, due to the placement of the crossover point, the gains diverge at low energies. This causes any errors in the measured effective temperature to be amplified at low energies. This is in contrast to the FL filter (Figure 6A) where the gain scales converge at low energies. Figure 9 shows the measured detector resolution as function of energy using FL (red) and ZP with a constant x_s (blue). Above 4 keV, ZP gives as good or better resolutions than FL. However, at low-energies, ZP performs worse due to the divergence of the gain scales. Note that the apparent increase of the resolution around 3 keV is due to poor knowledge of the intrinsic line shapes for Cl Kα and K Kα.

As an alternative to using a constant offset, we can let x_s vary with the environmental conditions such that the last two terms in Eq. 1 sum to zero. This will yield gain scales that have a crossover point at zero, same as with the full-length filters. This approach removes the problems with the crossover point, but requires us to accurately track how the baseline varies with time. We could use the baseline values computed from the average of the pre-trigger region of the pulse records (magenta points in Figure 5C). However, due to low statistics, these baseline values have a fairly large dispersion which gets transferred to the pulse heights if used as the basis for x_s. This leads to poorer resolutions than FL over the whole spectral range.

A better approach is to use an averaged baseline trend com-

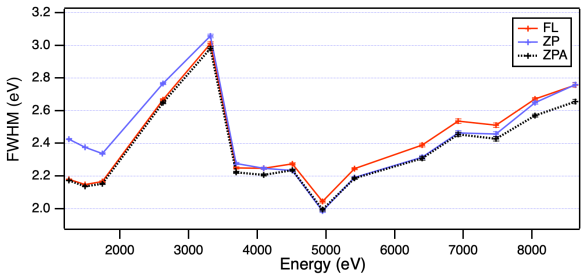

Fig. 9. Resolution of the 55.25 mK data set calibrated by interpolating the 55, 55.5, and 55.75 mK gains at Cr Kα: FL (red), ZP (blue), and ZPA (black dotted).

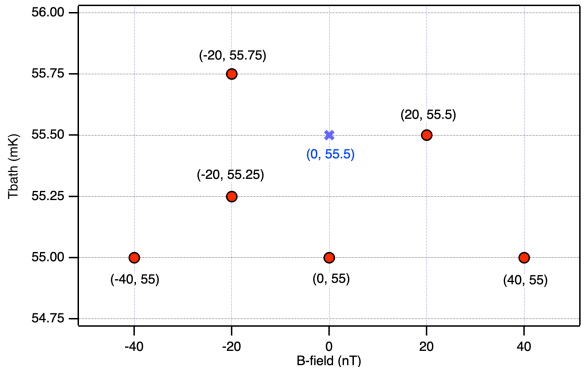

Fig. 10. Position of the 6 reference gain scales (red circles) for the energy calibration of the data set to be calibrated (blue cross) in the 2D parameter space of bath temperature and B-field.

puted from the pre-trigger values (black curve in Figure 5C). Using this as the basis for x_s yields the dotted, black curve in Figure 9 solving the poor-resolution problem at low-energies but still giving the improved resolutions at high energies. We denote this method as ZPA (0-padding adjusted).

VI. Calibration Results

For the energy calibration of X-IFU data, we are expecting to interpolate gain scales in a 2D parameter space (bath temperature and B-field) using 2nd-order, 2D Lagrange polynomials [7]. Such interpolation requires 6 reference gain scales and 2 fiducials (1 line + baseline or 2 lines). In Figure 10, we show the parameters of the reference gain scales (red) and the data set we are calibrating (blue). We calibrate the data set using two fiducial lines: Cr Kα (5.4 keV) and Cu Kα (8 keV), the same as intended for use by the MXS on Athena.

The 2-parameter calibration results (Figure 11) are very similar to what we obtained with the 1-parameter calibration on bath temperature (Figure 9). At high-energies, ZP (i.e., fixed x_s) delivers improved resolutions compared to the full-length filter (FL), but the gain crossover point in temperature space degrades the resolution at low energies. ZPA solves the low-energy problem but still retains the improved resolution at high energies. We note that the absolute energies of the calibration lines from ZPA are in good agreement with FL (within 0.05 eV), but the ZP energies are systematically off by $\sim$0.1 eV at low energies.

In Figure 12, we show the computed effective parameters from FL (red) and ZP (blue); the ZPA parameters are in good

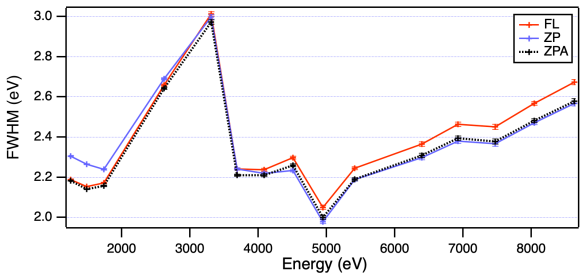

Fig. 11. Comparison of the instrument resolution using the 2-parameter calibration method: FL (red), ZP (blue), and ZPA (black dotted).

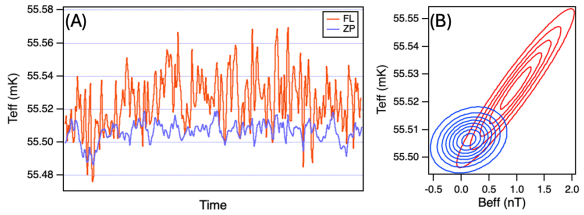

Fig. 12. (A) Comparison of $T_{\rm eff}$ from FL (red) and ZP (blue) calibration results. (B) Correlation between $T_{\rm eff}$ and B-field parameters. To avoid clutter, the ZPA results are not shown, but they are in good agreement with FL.

agreement with FL and are not shown. The ZP parameters show less dispersion and are closer to the expected values of $T_{\rm eff}$ = 55.5 mK and $B_{\rm eff}$ = 0 nT than the FL and ZPA results. This alone might suggest that the ZP results are better than the FL/ZPA results since less variation in, e.g., $T_{\rm eff}$ implies less variation in the gain curves for a fixed $B_{\rm eff}$. However, in panel B, we see that $T_{\rm eff}$ and $B_{\rm eff}$ for FL/ZPA are highly correlated. Given this correlation and the better overall resolution of ZPA over ZP, the strong correlation suggests that there are extended regions in the 2D parameter space of $T_{\rm eff}$ and $B_{\rm eff}$ that give similar shapes of the interpolated gain curves. It is important to note that this correlation is a numerical artifact and does not imply that the actual temperature and B-field at the detector are correlated. The low correlation seen for ZP indicates that both parameters are needed in order to simultaneously track the time-dependent drift of the calibration line positions and the baseline, which is consistent with the increased baseline dependence observed in the ZP optimally-filtered pulse heights (Figure 4). In contrast, for FL and ZPA, the baseline dependence has largely been removed from the pulse heights. So, the difference in the correlations actually implies that 2-parameter calibration is more useful for ZP than FL/ZPA. This can be confirmed by comparing the improvement in the resolutions going from the 1-parameter calibration (Figure 9) to the 2-parameter calibration (Figure 11) where ZP results change more than ZPA. However, ZPA still gives a better overall resolution than ZP in both cases.

VII. Conclusion

We have demonstrated that the 0-padding method works well with measurements taken in a laboratory environment. We can successfully employ multi-parameter, non-linear gain calibration and obtain results consistent with, or better, than the full-length filter over the entire spectral range. Best results

from the 0-padding method are obtained when adjusting the 0-padded pulse heights based on an averaged time drift of the event baseline values (ZPA method). Better resolutions are also obtained when the time drift of the pulse heights is measured by grouping data from many pixels together instead of tracking each pixel separately (co-drifting).

Future plans include investigating the performance of ZPA under a variety of flight-like conditions. The main limitation of ZPA is the need to accurately track the time-dependence of the baseline. This is most challenging in the regime of high count rates where pile-up can make baseline measurements from the pre-trigger region of pulses unreliable. More work is needed to see if a baseline trend can be accurately measured under such conditions. For example, we will explore using periodic, untriggered baseline sampling to supplement our baseline knowledge.

REFERENCES

[1] K. Nandra *et al.*, "The hot and energetic universe: A white paper presenting the science theme motivating the athena+ mission," 2013.

[2] D. Barret *et al.*, "The athena x-ray integral field unit: a consolidated design for the system requirement review of the preliminary definition phase," *Experimental Astronomy*, vol. 55, no. 2, pp. 373–426, 2023.

[3] S. J. Smith *et al.*, "Development of the microcalorimeter detector for the Athena/X-ray Integral Field Unit," in *Space Telescopes and Instrumentation 2024: Ultraviolet to Gamma Ray*, J.-W. A. den Herder, S. Nikzad, and K. Nakazawa, Eds., vol. 13093, International Society for Optics and Photonics. SPIE, 2024, p. 130930V.

[4] J. W. Fowler *et al.*, "The practice of pulse processing," *Journal of Low Temperature Physics*, vol. 184, no. 1, pp. 374–381, 2016.

[5] M. T. Ceballos *et al.*, "The first cut is the cheapest: optimizing athena/x-ifu-like tes detectors resolution by filter truncation," *Experimental Astronomy*, vol. 57, no. 2, p. 14, 2024.

[6] S. J. Smith *et al.*, "Correcting gain drift in tes detectors for future x-ray satellite missions," *IEEE Transactions on Applied Superconductivity*, vol. 33, no. 5, pp. 1–6, 2023, art no. 2101006.

[7] E. Cucchetti *et al.*, "Advanced energy scale correction techniques for the x-ray transition edge sensors of the athena mission," *Journal of Low Temperature Physics*, vol. 216, no. 1, pp. 292–301, 2024.

[8] S. J. Smith *et al.*, "Performance of a broad-band, high-resolution, transition-edge sensor spectrometer for x-ray astrophysics," *IEEE Transactions on Applied Superconductivity*, vol. 31, no. 5, pp. 1–6, 2021, art no. 2100806.

[9] M. Durkin *et al.*, "Demonstration of athena x-ifu compatible 40-row time-division-multiplexed readout," *IEEE Transactions on Applied Superconductivity*, vol. 29, no. 5, pp. 1–5, 2019, art no. 2101005.

[10] M. E. Eckart *et al.*, "Ground calibration of the Astro-H (Hitomi) soft x-ray spectrometer," *Journal of Astronomical Telescopes, Instruments, and Systems*, vol. 4, no. 2, p. 021406, 2018.

[11] F. S. Porter *et al.*, "Temporal gain correction for x-ray calorimeter spectrometers," *Journal of Low Temperature Physics*, vol. 184, no. 1, pp. 498–504, 2016.

[12] E. Cucchetti *et al.*, "Energy scale calibration and drift correction of the X-IFU," in *Space Telescopes and Instrumentation 2018: Ultraviolet to Gamma Ray*, J.-W. A. den Herder, S. Nikzad, and K. Nakazawa, Eds., vol. 10699, International Society for Optics and Photonics. SPIE, 2018, p. 106994M.